



## Article

# New Insights into Ice Avalanche-Induced Debris Flows in Southeastern Tibet Using SAR Technology

Siyuan Luo <sup>1</sup>, Junnan Xiong <sup>1,2,\*</sup>, Shuang Liu <sup>3</sup>, Kaiheng Hu <sup>3</sup>, Weiming Cheng <sup>2</sup>, Jun Liu <sup>1</sup>, Yufeng He <sup>1</sup>, Huaizhang Sun <sup>4</sup>, Xingjie Cui <sup>1</sup> and Xin Wang <sup>1</sup>

<sup>1</sup> School of Civil Engineering and Geomatics, Southwest Petroleum University, Chengdu 610500, China; 202202000947@stu.swpu.edu.cn (S.L.); 201922000655@stu.swpu.edu.cn (J.L.); 201922000656@stu.swpu.edu.cn (Y.H.); 202022000943@stu.swpu.edu.cn (X.C.); 202022000951@stu.swpu.edu.cn (X.W.)

<sup>2</sup> State Key Laboratory of Resources and Environmental Information System, Institute of Geographic Sciences and Natural Resources Research, Chinese Academy of Sciences, Beijing 100101, China; chengwm@reis.ac.cn

<sup>3</sup> Institute of Mountain Hazards and Environment, Chinese Academy of Sciences, Chengdu 610041, China; liushuang@imde.ac.cn (S.L.); khhu@imde.ac.cn (K.H.)

<sup>4</sup> School of Geography and Planning, Sun Yat-sen University, Guangzhou 510275, China; sunhzh5@mail2.sysu.edu.cn

\* Correspondence: xiongjn@swpu.edu.cn

**Abstract:** Drastic climate change has led to glacier retreat in southeastern Tibet, and the increased frequency and magnitude of heavy rainfall and intense snow melting have intensified the risk of ice avalanche-induced debris flows in this region. To prevent and mitigate such hazards, it is important to derive the pre-disaster evolutionary characteristics of glacial debris flows and understand their triggering mechanisms. However, ice avalanche-induced debris flows mostly occur in remote alpine mountainous areas that are hard for humans to reach, which makes it extremely difficult to conduct continuous ground surveys and optical remote sensing monitoring. To this end, synthetic aperture radar (SAR) images were used in this study to detect and analyze the pre-disaster deformation characteristics and spatial evolution in the Sedongpu Basin and to detect changes in the snowmelt in the basin in order to improve our understanding of the triggering mechanism of the ice avalanche-induced debris flows in this region. The results revealed that the maximum average deformation rate in the basin reached 57.3 mm/year during the monitoring period from January 2016 to October 2018. The deformation displacement in the gully where the ice avalanche source area was located was intimately correlated with the summer snowmelt and rainfall and was characterized by seasonal accumulation. Clear acceleration of the deformation was detected after both the most recent earthquake and the strong rainfall and snowmelt processes in the summer of 2018. This suggests that earthquakes, snowmelt, and rainfall were significant triggers of the Sedongpu ice avalanche-induced debris flows. The results of this study provide new insights into the genesis of the Sedongpu ice avalanche-induced debris flows, which could assist in disaster warning and prevention in alpine mountain regions.

**Keywords:** SAR; time-series InSAR; deformation monitoring; snowmelt; Sentinel-1



**Citation:** Luo, S.; Xiong, J.; Liu, S.; Hu, K.; Cheng, W.; Liu, J.; He, Y.; Sun, H.; Cui, X.; Wang, X. New Insights into Ice Avalanche-Induced Debris Flows in Southeastern Tibet Using SAR Technology. *Remote Sens.* **2022**, *14*, 2603. <https://doi.org/10.3390/rs14112603>

Academic Editor: Timo Balz

Received: 28 April 2022

Accepted: 27 May 2022

Published: 29 May 2022

**Publisher's Note:** MDPI stays neutral with regard to jurisdictional claims in published maps and institutional affiliations.



**Copyright:** © 2022 by the authors. Licensee MDPI, Basel, Switzerland. This article is an open access article distributed under the terms and conditions of the Creative Commons Attribution (CC BY) license (<https://creativecommons.org/licenses/by/4.0/>).

## 1. Introduction

Known as the third pole of the Earth and the water tower of Asia, the Tibetan Plateau is an important ecosystem and provides vital resources for the survival of thousands of humans. Unfortunately, it is also one of the most ecologically vulnerable regions on the planet [1]. As one of the most sensitive regions to global climate change, the warming rate of the Tibetan Plateau has reached 0.3–0.4 °C/10a in recent decades, which is twice the global average during the same period [2]. In the context of drastic climate change, the glaciers in southern Tibet have exhibited a significant negative mass balance and an accelerated

trend of glacier retreat [3]. In addition, the steep terrain and active crustal movement in some regions have greatly reduced the overall stability of the glaciers, thus increasing the risk of glacial hazards [4]. New types of hazards such as glacial avalanches and their resulting disaster chains have become more prominent [5–7]. During 2007–2010, there were three periglacial debris flows in Tianmo Valley, all of which caused blockage of the Yarlung Zangbo River [8]. Since 2014, there have been nine blockages of the Yarlung Zangbo River in the Sedongpu Basin, five of which were caused by debris flows triggered by ice avalanches, with the most serious one occurring on 17 October 2018 [9]. In fact, the snow in the basin melted dramatically in the summer, providing hardly any areas for ice accumulation in rock glaciers under the effects of climate warming [10]. Subsequent glacier thinning and retreat have exposed the steep rock walls below the glacier, separating the glacier from the rock and leading to the formation of fissures [11–13]. A powerful 6.9-magnitude earthquake struck near the Sedongpu Basin on 18 November 2017, causing significant ground motion within the basin, which affects the stability of the rock slopes and promotes the occurrence of large ice avalanches [13]. In order to prevent the formation of such disaster chains, disaster prevention measures should be implemented at the source [14]. The pre-disaster surface deformation and seasonal snowmelt in the basin, as well as their correlation with external factors, can hopefully reveal the triggering factors and failure mechanisms, helping us to manage the threat of ice avalanche hazard chains from the source.

In fact, the application of traditional deformation observation tools for continuous in situ measurements in glacial areas is very limited due to the difficulties of accessing alpine mountains [15]. Optical remote sensing technology is widely used in geological disaster investigation, monitoring, and prevention [16–18]. However, optical remote sensing is often hindered by severe weather conditions, especially in high mountain valley areas [19]. With its advantages of high accuracy, dynamic continuity, and ability to overcome adverse weather conditions, phase-based Interferometric Synthetic Aperture Radar (InSAR) can measure the displacement in the satellite's line-of-sight (LOS) direction [20–22] and has become an essential tool for monitoring surface displacement [23–25]. Moreover, landslide types and failure modes can be inferred by characterizing the changes in the surface deformation based on historical deformation recovery, which provides significant guidance for debris flow and landslide risk reduction efforts. Dong et al. [26] and Intrieri et al. [27] acquired the time series deformation before the collapse of the Xinmo landslide based on Sentinel-1 data. Based on this, Kang et al. [28] found that the maximum deformation occurred in the middle of the source area after analyzing the deformation characteristics during the landslide's development. Furthermore, Zhang et al. [29] addressed the developmental mode of the Suertou earthflow using Advanced Land Observing Satellite (ALOS) Phased Array L-band Synthetic Aperture Radar (PALSAR) dataset, revealing the accelerating effects of precipitation and earthquakes on the deformation. Zhang, et al. [30] used the small baseline subsets (SBAS) method to investigate the Bailong River Basin in order to demonstrate the reliability of the SBAS method for detecting and monitoring geohazards in basins with rugged terrain. Glacier retreat can seriously affect rock slope stability, increasing the frequency of ice avalanches and the risk of rockfalls [31]. Therefore, due to the advantages of InSAR technology in surface deformation detection in remote mountainous areas, its application to deformation monitoring in glacial basins can assist in the study of rock slope stability under glacial retreat.

Monitoring alpine seasonal snowmelt, especially wet snow, is crucial for research on mountain hydrology, ecosystems, and geohazard risk prediction [32]. Due to the difficulty of acquiring optical data not obscured by clouds, most studies on geohazards in alpine mountains have ignored the effect of mountain snowmelt on the hazard development process. In fact, the melting of snow and ice, which is exacerbated by climate warming, is permanently altering the magnitude and frequency of cryospheric hazards [33]. The melting of snow may trigger translational sliding of the active layer of ice, which may trigger landslides or provide loose deposits and liquid water for triggering debris flows [34]. Therefore, it is necessary to consider the effect of seasonal snowmelt when studying

the triggering factors of alpine hazards. Airborne Ground Penetrating Radar has the advantage of being less susceptible to terrain and quick survey to study glaciers and snow cover [35,36], but it is still a challenge to apply it to alpine mountains for seasonal snowmelt detection. The C-band radar datasets acquired by the Sentinel-1 satellite have facilitated the study of this issue. Numerous studies have used SAR, which is highly sensitive to the liquid water content of snow, is insensitive to clouds, and has a high spatial resolution, to achieve detection of the extent of wet snow in alpine regions [37–40]. Incorporating seasonal snowmelt detection into the monitoring of geological hazards in alpine regions and conducting quantitative analysis of this factor will help identify the extent of snowmelt accumulation in remote and hazardous glacier areas, thus improving the monitoring and early warning of geological hazards in alpine regions.

Accordingly, in order to explore the ability of SAR to obtain disaster precursor information in alpine mountains, we selected the Sedongpu Basin, which contains the Yarlung Zangbo River, as the study area. InSAR was used to retrieve the pre-disaster deformation, and the variations in the snowmelt were calculated using SAR image change detection, which overcomes the limitations of traditional deformation observation methods and optical remote sensing. The time series of the InSAR deformation and snowmelt changes were also analyzed in terms of the topography, seismic records, and historical rainfall records to determine the genesis of the Sedongpu ice avalanche-induced debris flows.

## 2. Study Area and Data Sources

### 2.1. Study Area

On 17 October 2018, massive ice avalanche-induced debris flows occurred in the Sedongpu Basin on the left bank of the Yarlung Zangbo River, 6 km downstream of Gala Village, Pai Town, Milin County, Tibet (Figure 1). Eventually, a barrier dam was formed and blocked the Yarlung Zangbo River. The Sedongpu Basin has an area of 66.61 km<sup>2</sup>. The highest point in the basin is the main peak of Gyala Peri Peak (7294 m), and the lowest point is 2746 m, with a large difference of 4548 m. The average elevation is 4540 m. The upper and lower parts of the Sedongpu Basin are steep, while the central part of the basin is relatively gentle. The average slope in the Sedongpu Basin is 33.84°, and more than 60% of the basin has a slope of greater than 30°, which provides favorable topographic conditions for the occurrence of debris flows. The study area is located at the eastern end of the Himalayas, close to the Yarlung Zangbo suture zone. It is affected by the tectonic stresses in the Himalayas and the frequent seismic activity in the vicinity, which results in poor stability in this region. The stratigraphy of the basin consists of the Namjagbarwa Group, and the bedrock exposed in the region is mainly Proterozoic gneiss and schist. Affected by glaciation and strong physical weathering, the surface rocks and soil are loose and broken, forming a large number of loose accumulation layers on the slopes and in the valley, which constitute the main sources of the solid components of the debris flows. The rainfall in the study area is mostly concentrated from June to September, during which heavy and torrential rainfall occurs frequently in the Yarlung Zangbo River Basin, accounting for more than 82% of the annual rainfall. The highest temperatures occur from May to September [41]. During this period, the strong melting of snow and ice exposes a large amount of moraine material beneath the glaciers at the surface, providing a rich source of debris flow material. In addition, the melt water of the ice and snow provides a water source for the occurrence of debris flows. A large number of marine glaciers are distributed in the Yarlung Zangbo Bend area. Compared with continental glaciers, marine glaciers have a fast movement rate and intense cumulative ablation. The glaciers developed in the Sedongpu Basin are typical marine glaciers, which are more prone to ice avalanches under the background of global warming [42].

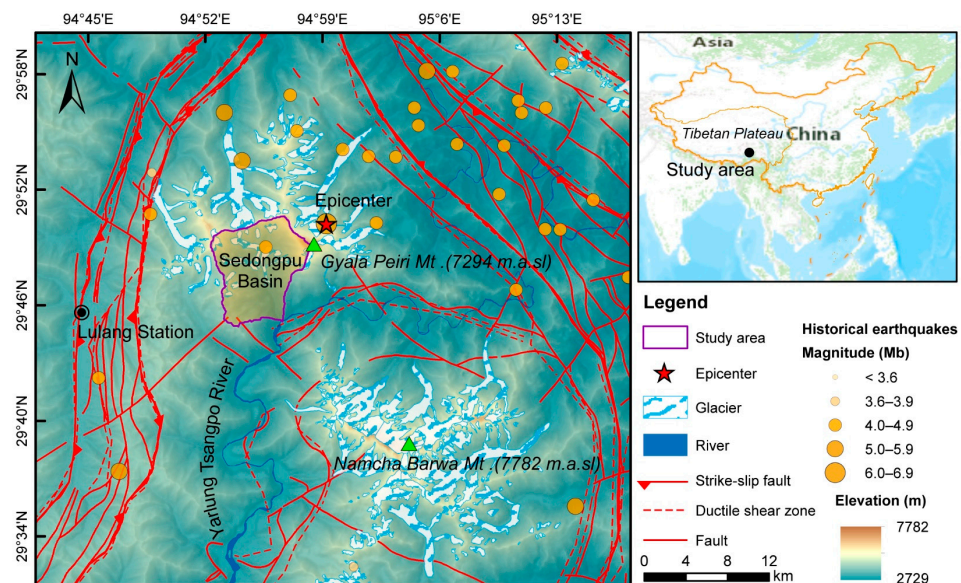


**Figure 1.** Geographic location and main surrounding tectonic features of the Sedongpu Basin in southeastern Tibet. The geologic structure of the study area was derived from a 25 W geologic map provided by the National Geological Archives of China (<http://www.ngac.org.cn/>, accessed on 5 May 2022). The circles represent earthquakes and aftershocks that occurred since 1950, and the historical seismic data were obtained from the USGS (<https://earthquake.usgs.gov/>, accessed on 24 March 2022).

## 2.2. Data Sources

In this study, a total of 73 descending and 62 ascending Sentinel-1A/B SAR images acquired by the European Space Agency (ESA) from October 2014 to October 2018 were used to monitor the time series of the deformation and snow area changes in the Sedongpu Basin. Among them, the SAR images from October 2016 to February 2017 were acquired from Sentinel-1B (6 in total), and all of the remaining images were acquired by Sentinel-1A. The Sentinel-1A/B satellite acquired data in the single-polarization (VV) mode covering the study area between October 2014 and February 2017 and started to acquire data in dual-polarization (VV+VH) mode in March 2017. Thus, for all of the selected SAR images, all of the processing was performed using the VV polarization mode. In addition, precise orbit ephemerides files (POEORBs) provided by the ESA were used to correct the orbital information and to remove systematic errors due to orbital errors. Moreover, the Advanced Spaceborne Thermal Emission and Reflection Radiometer (ASTER) global digital elevation model (GDEM) with a spatial resolution of approximately 30 m (1 arc-sec) was used for the SAR image registration and the removal of the topographic phase from the interferograms. The temperature and precipitation data were obtained from nearby meteorological stations. The main parameters of the satellites used in this article are presented in Table 1.

**Table 1.** Specific parameter information related to Sentinel-1A/B SAR images and ASTER GDEM data.

Data	Parameter	Description
Sentinel-1A/B	Orbit direction	Descending/Ascending
	Product type	SLC
	Polarization mode	VV
	Radar wavelength	5.6 cm
	Acquisition mode	IW
	Pixel spacing (azimuth × range)	13.96 m × 2.32 m
	Acquisition period	29 October 2014–13 October 2018
ASTER GDEM	Resolution	30 m

### 3. Methodology

#### 3.1. Fundamental Principle of the SBAS Method

The SBAS-InSAR combines differential interferometric pairs by selecting appropriate spatial baseline and temporal baseline thresholds, and then, it uses linear deformation models to calculate the selected coherent target points, which can reduce the decorrelation effects and elevation and atmospheric errors in differential InSAR (DInSAR) processing while acquiring the surface deformation time series. In this section, the basic principle of the SBAS-InSAR is briefly summarized.

Assuming that  $N + 1$  SAR images covering the study area were acquired following the time series  $(t_0, \dots, t_i, \dots, t_N)$ , one of these images is selected as the master image, and all the images are co-registered to the master image. Reasonable thresholds are set for the spatial baseline and temporal baseline, and images below this threshold are divided into a group.  $M$  interferometric pairs can be generated via differential interferometry processing for each group of images.  $M$  satisfies the following inequality:

$$\frac{N + 1}{2} \leq M \leq \frac{N(N + 1)}{2} \tag{1}$$

For the  $j$ th differential interferogram generated from the SAR acquisitions at times  $t_A$  and  $t_B$  ( $t_A < t_B$ ), the phase of a generic pixel with azimuth and range coordinates of  $(x, r)$  can be expressed as follows [22,43]:

$$\begin{aligned} \delta\phi_j(x, r) &= \phi(t_B, x, r) - \phi(t_A, x, r) \\ &\approx \frac{4\pi}{\lambda} [d(t_B, x, r) - d(t_A, x, r)] + \Delta\phi_{topo} + \Delta\phi_{orb} + \Delta\phi_{atm} + \Delta\phi_{noise} \end{aligned} \tag{2}$$

where  $j \in (1, \dots, M)$ , and  $\lambda$  is the radar wavelength.  $d(t_A, x, r)$  and  $d(t_B, x, r)$  are the line-of-sight (LOS) cumulative deformations at times  $t_A$  and  $t_B$  relative to the initial time  $t_0$ , respectively, and at  $t_0$ ,  $d(t_0, x, r) \equiv 0$ .  $\Delta\phi_{topo}$  is the phase contributed by the topographic error, which is proportional to the perpendicular baseline and inversely proportional to the sine of the incidence angle.  $\Delta\phi_{orb}$  is the SAR satellite orbit error, which can be reduced using POEORBs.  $\Delta\phi_{atm}$  is the phase contribution related to the atmosphere. This correction is needed because when two interferometric SAR images are not simultaneously acquired, the different atmospheric humidity, temperature, and pressure of the two acquisitions have a significant effect on the interferometric phase.  $\Delta\phi_{noise}$  is the random noise phase, including the thermal noise and spatial decorrelation.

In order to acquire the deformation of each pixel in the differential interferogram in the time series, let  $\phi = [\phi(t_1), \phi(t_2), \dots, \phi(t_N)]^T$  be the  $N \times 1$  vector of unknown phase values associated with the deformation of the pixel under consideration, and let  $\delta\phi = [\delta\phi_1, \delta\phi_2, \dots, \delta\phi_M]^T$  be the  $M \times 1$  vector of the unwrapped phase values related to the differential interferograms. Then, a system of  $M$  equations with  $N$  unknowns can be written as follows:

$$A\phi = \delta\phi \tag{3}$$

In order to ensure the solution has the correct physical significance, the unknowns in Equation (3) are replaced by the mean phase velocity. Consequently, the new unknowns become

$$v^T = \left[ v_1 = \frac{\phi_1}{t_1 - t_0}, \dots, v_N = \frac{\phi_N - \phi_{N-1}}{t_N - t_{N-1}} \right] \tag{4}$$

Then, Equation (3) can be rewritten as follows:

$$Bv = \delta\phi \tag{5}$$

where  $B$  is an  $M \times N$  coefficient matrix. Finally, by applying the least-squares (LS) and singular value decomposition (SVD) methods to matrix  $B$ , the LOS cumulative displacement at the image acquisition time can be calculated.

The Environment for Visualizing Images (ENVI) and its SARscape module were used to process the SAR images of the study area. In order to generate interferometric pairs with high coherence, the maximum normal baseline and the maximum temporal baseline thresholds were set to 100 m and 72 days, respectively. As shown in Figure 2, the SAR image acquired on 17 May 2018 was selected as the super master image. In the interferometric process, the external ASTER GDEM was used to remove the topographic phase, and the noise phase was removed using the Goldstein filter [44]. Furthermore, a multi-look with  $1 \times 4$  in the azimuth and range directions was used to improve the signal-to-noise ratio and coherence in the interferogram. In order to improve the quality of the unwrapping, the unwrapping coherence threshold was set to 0.3, and the minimum-cost flow (MCF) algorithm [45] was used for the phase unwrapping. After removing 38 interferometric pairs with low coherence coefficients, we finally obtained 201 interferometric pairs for the subsequent time series analysis. During the inversion of the surface deformation time series, 64 ground control points (GCPs) were selected in the non-deformation area and were used to remove the atmospheric phase and eliminate the residual topographic phase. Since the atmospheric component has a high spatial correlation and a low temporal correlation, the effect of the atmospheric delay can be alleviated by applying a spatial–temporal filter with an atmosphere high path size of 365 days and an atmosphere low path size of 1200 m [46,47]. After that, the final average modeled displacement was computed on the time series.

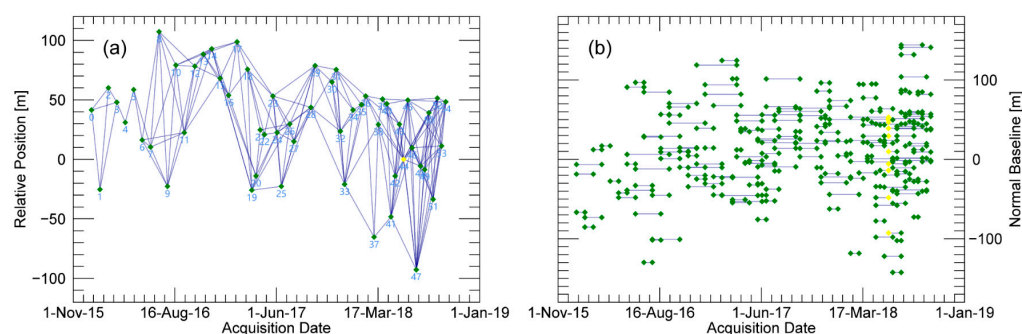


**Figure 2.** Spatial and temporal baselines of the Sentinel-1A data used in this study. (a) The acquisition date and relative position of each SAR image. (b) Temporal baseline of the interferometric pair. The yellow point indicates the super master image, and the connecting line indicates that the two images form an interferometric pair.

### 3.2. Extraction of Wet Snow Cover Area

The reduced backscattering coefficient ( $\sigma^0$ ) of surfaces covered by wet snow compared to those covered by no snow or dry snow provides the basis for mapping the snowmelt areas [37,40,48,49]. In this study, the ratio of the backscattering coefficient of the SAR detection image with melting snow ( $\sigma_{snow}^0$ ) to the reference image ( $\sigma_{ref}^0$ ) was used to detect the snowmelt areas with reduced backscatter signals, and the snow-covered and non-snow-covered surfaces were segmented based on the threshold. Selecting a suitable reference image is crucial for image classification. The reference image used in this study was an average of multiple SAR images from scenes covered by no snow or dry snow during autumn and winter. Using multiple images to create a reference image can reduce speckles and effectively suppress the effect of the backscattering variations in the reference scene on different dates [39].

Several pre-processing steps are required for each SAR image involved in the calculation of the wet snow image. First, all of the SAR images after multi-look processing were accurately co-registered to the pre-selected master image for the same orbit. Multi-temporal radar image filters, which make the information complementary by constructing optimal linear combinations of multiple time-series images, were used to reduce the inherent image speckle noise. After the radiation calibration process was used to calculate the backscattering intensity, each pixel was converted from the slant range geometry to the map projection.

In order to avoid the effect of the incidence angle, shadows, and the overlap phenomenon on the backscattering coefficient, the shadows, layover areas, foreshortening areas, and the areas with incidence angles of less than  $18^\circ$  or greater than  $78^\circ$  were masked. Then, we calculated the binary snow map by combining the ratios of the ascending and descending tracks according to the values of the local incidence angle using the algorithm described below [37]:

$$\begin{cases} \text{if } (L = \text{TRUE or } S = \text{TRUE or } \theta_i < 18^\circ \text{ or } \theta_i > 78^\circ) & \rightarrow \text{no information} \\ \text{else if } (\sigma_{\text{snow}}^0 / \sigma_{\text{ref}}^0 < \text{TR}) & \rightarrow \text{wet snow} \\ \text{else} & \rightarrow \text{snow free} \end{cases} \quad (6)$$

where  $L$  and  $S$  are the layover and shadow pixels, respectively, and  $\theta_i$  is the local incidence angle. TR is the threshold for computing the ascending and descending wet snow maps. A threshold of  $-3$  dB often underestimates the wet snow extent, especially near the snow line, so we used  $-2$  dB as the threshold for detecting wet snow. Since C-band electromagnetic waves can easily penetrate dry snow, the backscatter obtained by the SAR is mainly from the rough surface scattering at the soil–snow interface covered by dry snow, so it is very difficult to detect dry snow based on image changes [50]. The seasonal snowmelt variability within the Sedongpu Basin is reflected well by the mapping of the wet snow time series. Therefore, the dry snow was excluded in this study, and only the changes in the wet snow were considered.

## 4. Results and Analysis

### 4.1. Precursory Movements of Ice Avalanche-Induced Debris Flows Measured via Time Series InSAR Analysis

In order to obtain the surface deformation results for the Sedongpu Basin, the ascending and descending track data would ideally be used in combination. However, due to the effect of the terrain factors, the SAR images acquired in the ascending orbit were severely limited by layover and shadows, therefore, only the descending data could be used in this study. Based on the SBAS-InSAR technique, the average surface deformation rate in the Sedongpu Basin during the period from January 2016 to September 2018 was obtained. In order to avoid the effect of the incidence angle of the satellite sensor on the LOS direction measurements [51], we removed the shadows, layover areas, and foreshortening areas during the data processing to ensure the reliability of the results [52]. The pre-disaster displacement measurements in the Sedongpu Basin were superimposed on the topography (Figure 3). The positive values indicate that the surface deformation movement was along the LOS direction towards the satellite, and the negative values indicate that the movement was along the LOS direction away from the satellite. Due to the dense vegetation cover, only a limited number of coherent targets were detected. Most of the identified coherent points were distributed in the source area at the top of the mountain, corresponding to the exposed rocks and gravel. As can be seen from Figure 3, for most of the detected points in the Sedongpu Basin, the absolute values of the displacement rates were less than  $10$  mm/year, but in the source area where the ice avalanches originated and in the gully where they flowed, as well as the area where deposits accumulated, some of the detection points were relatively active, with the absolute value of the displacement rate being greater than  $25$  mm/year. Moreover, the spatial pattern of the deformation area was highly consistent with the source area detected during the field survey and using optical remote sensing images [7,53], which undoubtedly confirms that slow slope deformation occurred in the Sedongpu Basin during the acquisition of the SAR data and the effectiveness of the InSAR analysis in the inversion of the precursory movement of the landslide.

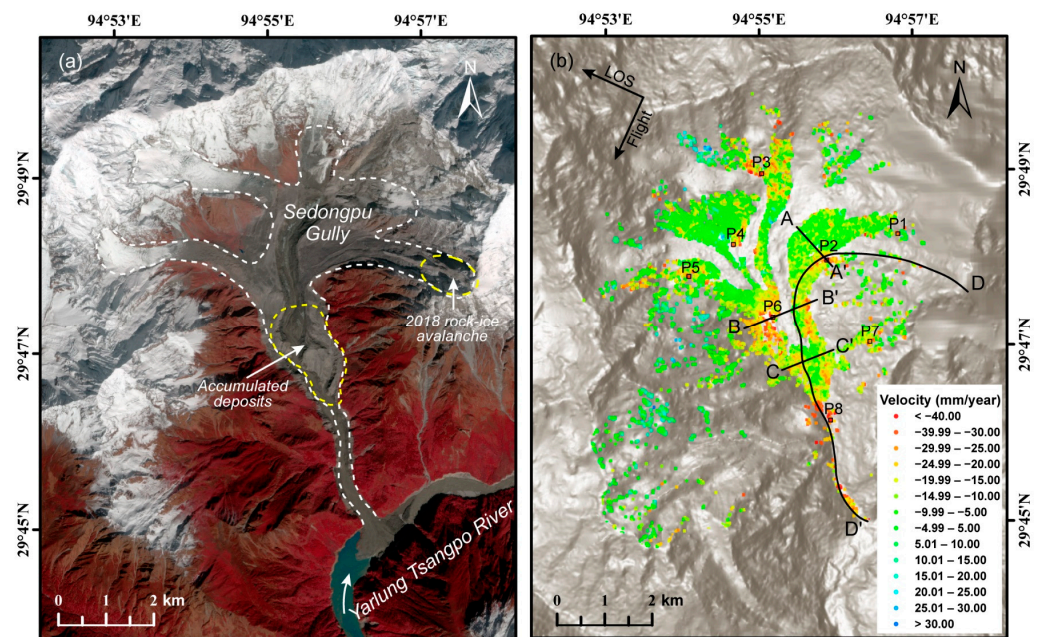


**Figure 3.** (a) Sentinel-2 image of Sedongpu Gully on 31 October 2018. The yellow dashed lines denote the source area where the ice avalanche occurred and the accumulation area of the pre-disaster deposits. (b) Map showing the annual average deformation rate in the LOS direction obtained by analyzing 55 Sentinel-1A descending-track images using the InSAR technique. Solid lines AA', BB', CC', and DD' indicate the locations of the profiles, which will be discussed later.

To further analyze the evolution of the displacement with time, we uniformly selected 10 representative regions and plotted their time series displacements. The time-series deformation curves illustrate the evolution of the deformation during the entire monitoring period. They can highlight the potential changes in the displacement that occurred during the monitoring period and can clearly illustrate whether the displacement motion was in a slow deformation or accelerated state, which is crucial to determining and studying the pre-disaster motion pattern in the Sedongpu Basin. In order to reduce the error and improve the robustness of the results, we chose an area of  $100\text{ m} \times 100\text{ m}$  as the main deformation area, which was centered on the point where the deformation rate was most prominent. The mean value of the LOS displacement time series in each selected area was estimated, and the standard deviation of all of the selected points in the deformation area at each SAR observation was calculated to analyze the inhomogeneity of the motion.

As shown in Table 2, among the selected deformation regions, the cumulative deformation in P8 was the largest, followed by that in P2. P8 was located in the lower part of the deposit accumulation zone, and a large number of coherent points with an average deformation rate of greater than  $-25\text{ mm/year}$  were distributed near this region, as well as the most obviously deformed region in the Sedongpu gully, which had a maximum cumulative deformation of  $-137.52\text{ mm}$ . By analyzing region P6, which was located in the upper part of the deposit accumulation zone, it was found that the average deformation rate varied, i.e., it was in an unstable state. The average deformation rate exceeded  $-25\text{ mm/year}$  and was clearly distinguishable from the boundary of the stable zone. However, after analyzing the time series deformation curve (Figure 4), it was found that it had been in a stage of uniform deformation. Region P2, which was located below the ice avalanche source area, underwent strong displacement, with a maximum displacement rate of about  $-48.52\text{ mm/year}$ . We found that all of the selected areas exhibited different levels of accelerated subsidence at the beginning of March 2018, among which regions P1, P3, P5 and P7 had the most obvious subsidence trends. The areas with obvious subsidence trends were all located at the tops of the branch gullies bordering the snow area, and the strong melting of snow and the delayed effect of the 2017 Nyingchi earthquake may have been responsible for this distribution.

**Table 2.** Average deformation rate, maximum deformation rate, maximum cumulative deformation in the LOS direction and whether sliding occurred in all of the selected deformation regions.

Number	Average Deformation (mm/Year)	Maximum Deformation (mm/Year)	Maximum Cumulative Displacement (mm)	Slide
P1	−30.90	−32.52	−76.05	Yes
P2	−45.21	−48.52	−120.72	Yes
P3	−40.28	−44.39	−97.69	No
P4	−34.93	−37.05	−112.46	No
P5	−35.04	−40.46	−101.32	No
P6	−34.64	−37.73	−93.86	No
P7	−28.76	−31.14	−79.79	No
P8	−48.44	−51.99	−137.52	Yes

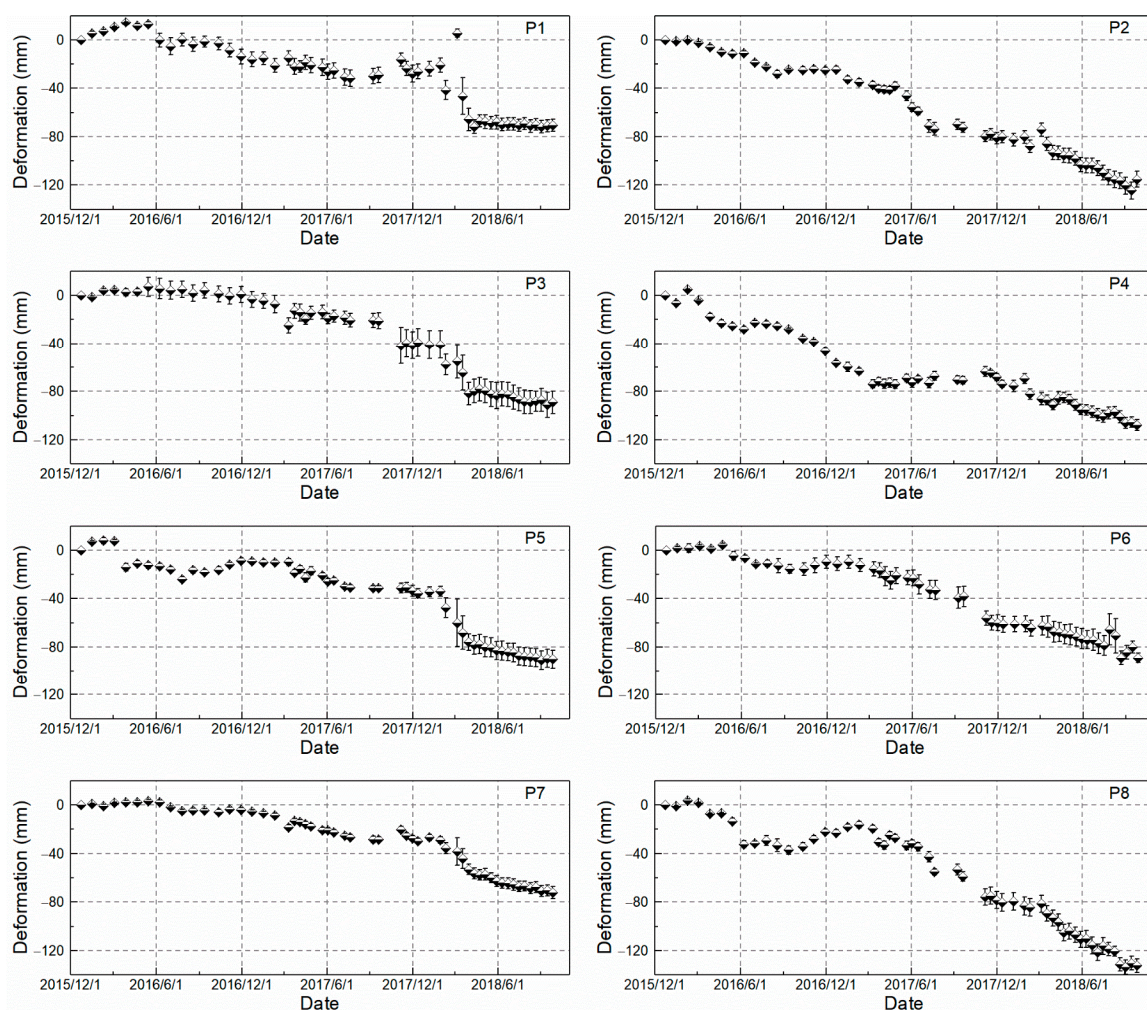


**Figure 4.** The time series of the cumulative deformation in regions P1–P8. The vertical error bars indicate the standard deviation of the cumulative amount of deformation in each selected region.

The accumulation of the displacements in the time dimension can help us better analyze the pre-disaster evolution from instability to failure in the Sedongpu Basin. We plotted the cumulative displacement in the LOS direction of the branch gully where the source area of the ice avalanche was located for 16 selected acquisitions that collapsed first (Figure 5), including the last seven images acquired near the time of the collapse. A total of 7109 points were detected in this source area. There were 708 points in this area with mean deformation rates of greater than  $-20$  mm/year in the LOS direction, and the

maximum deformation rate reached  $-57.29$  mm/year. The distribution of the surface deformation clearly delineated the unstable areas in the source zone in the Sedongpu Basin. The precursor deformation in the branch gully exhibited distinct spatial and temporal deformation characteristics. The cumulative deformation increased significantly in 2018 compared to that in previous years, and an accelerating displacement trend along the LOS direction away from the satellite was clearly observed.

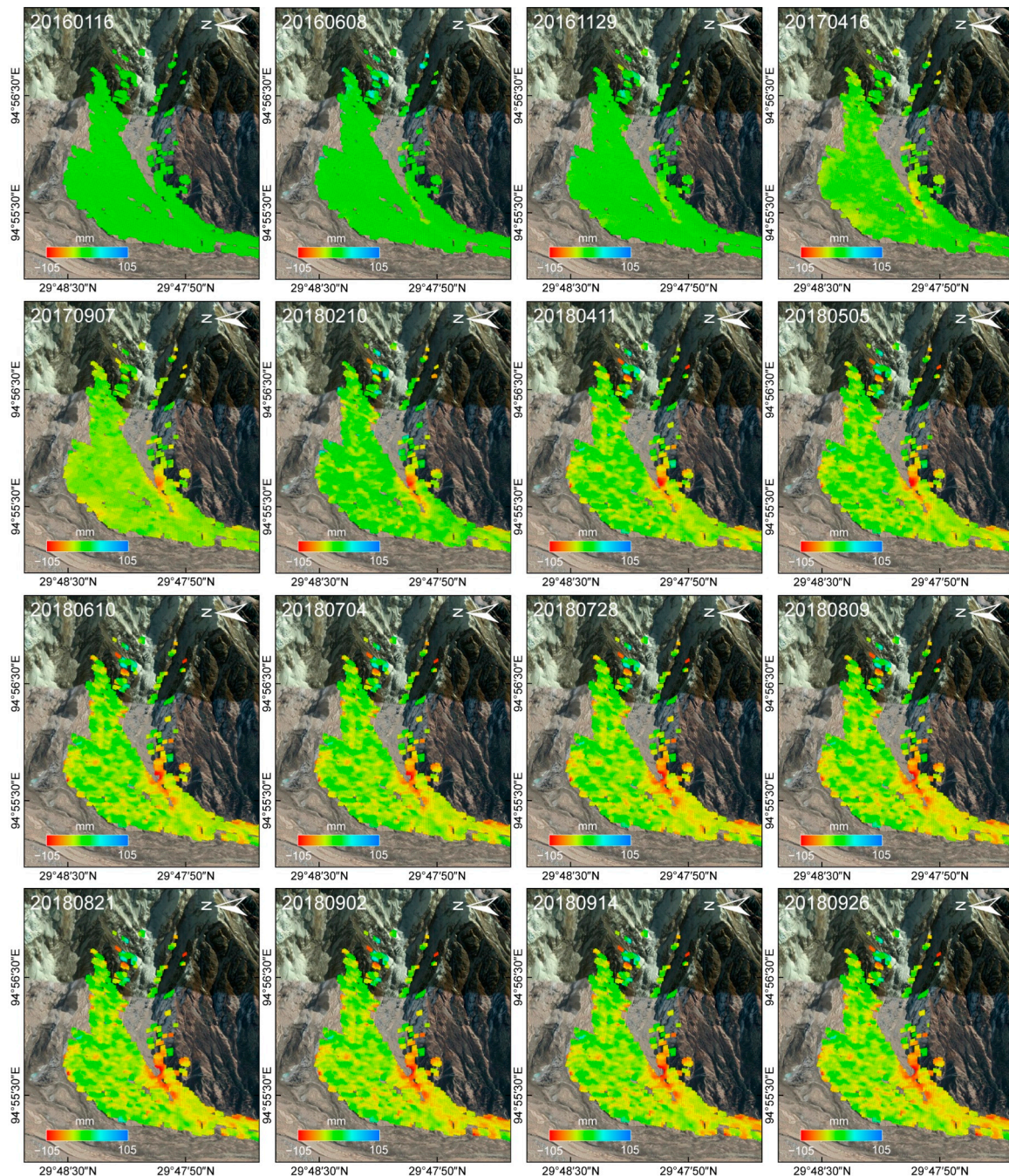


**Figure 5.** The cumulative deformation time series in the LOS direction for the source area where the first ice avalanche occurred in 2018 superimposed on Google Earth™ images. The first image was acquired in January 2016. The location of the ice avalanche source area was shown in Figure 3.

For further analysis of the spatiotemporal evolution of the deformation in the channel, we extracted the cumulative deformation along profiles AA', BB', and CC'. Figure 6a–c show the deformation time series of sections AA', BB', and CC' in the LOS direction,

respectively. The topography is shown below as a reference, and the positions of the profiles are marked in Figure 3. During the monitoring period, all three cross-sections underwent obvious deformation, and the maximum cumulative deformation exceeded 100 mm; however, their deformation characteristics were different. The deformation of section AA' gradually increased from the slope on both sides to the bottom of the slope, and the largest deformation occurred in the branch gully where region P2 was located. In contrast, the obvious deformation in both section BB' and CC' mainly occurred on the slope. At the beginning of 2018, the entirety of section BB' exhibited prominent deformation, and there was a large increase in the deformation of section AA'. The Nyingchi earthquake may have been the main cause of these changes, and they are sufficient to demonstrate that the base of the slope in the ice avalanche's source area was in an extremely unstable state.

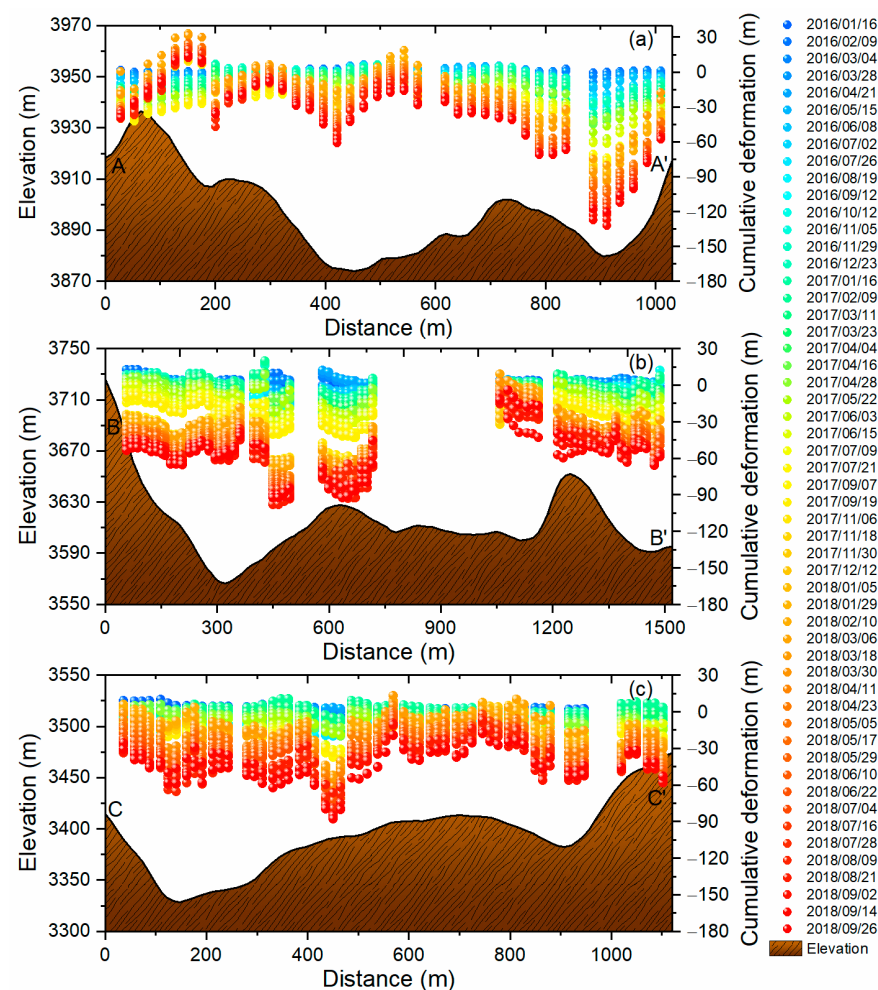


**Figure 6.** The cumulative time series of the deformation along profiles (a) AA', (b) BB' and (c) CC'.

#### 4.2. Spatiotemporal Changes in the Wet Snow Area during the Snowmelt Season

The Sedongpu ice avalanche-induced debris flows did not arouse widespread concern before the disaster because of its hard-to-access location and distance from human settlements. According to research speculation, glacier retreat and seasonal snowmelt may have been the main driving factors of this disaster [53]. The facilitation of the Sedongpu ice avalanche-induced debris flows by glacier retreat was demonstrated [13], but the effects of seasonal snowmelt have not been clearly interpreted. In order to explore the relationship between the seasonal snowmelt and surface deformation, we need to clearly understand the changes in the snow cover during the snowmelt season. Based on the method described in Section 3.2, we used a threshold of  $-2$  dB to extract the snow area within the Sedongpu Basin to avoid underestimating the area of wet snow. To reduce the effects of the terrain

factors and the loss of backscattered information from the SAR images of the mountainous areas, the shadow and layover pixels of the ascending and descending images were masked, and we used a combination of ascending and descending images to reduce the loss of image information such as that due to layover and shadows. Ascending and descending images acquired at adjacent times can effectively reveal the state of the snowpack. However, due to the limitation of SAR data acquisition, in this study, ascending and descending images acquired at the nearest times with an interval of seven days were used for the mapping of the wet snow area.

As shown in Figure 7, we mapped the monthly dynamics of the wet snow in the Sedongpu Basin during the snowmelt season from 2015 to 2018, with dark blue representing the areas covered by wet snow, orange representing an increase in wet snow, and light blue representing a decrease in wet snow. In addition, we calculated the wet snow area in each period (Table 3). During this period, the observed largest area of wet snow was 13.57 km<sup>2</sup> in early May 2016, and the smallest area was 3.67 km<sup>2</sup> at the end of July 2015.

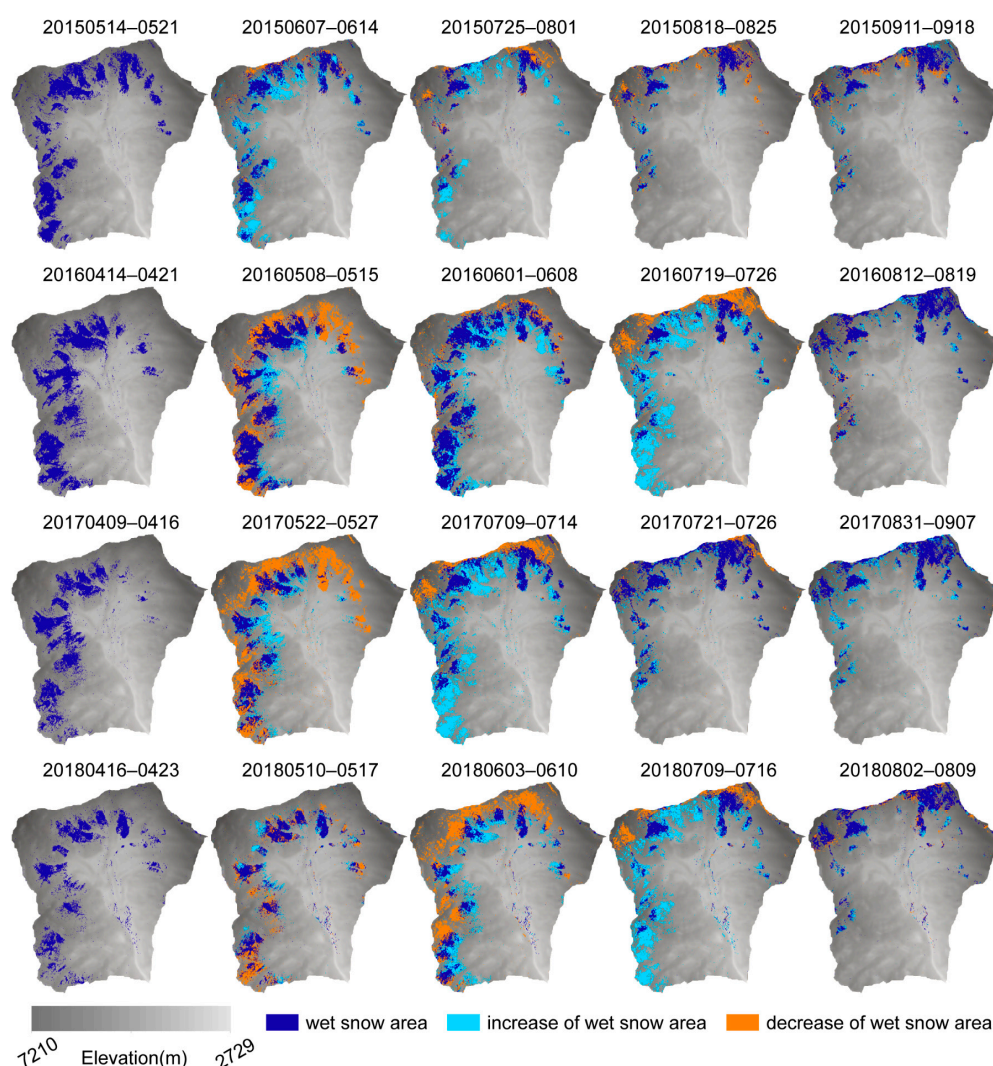


**Figure 7.** Maps of snowmelt area variations in the Sedongpu Basin. The SAR image dates used to detect the wet snow changes are marked on each map. Dark blue: the area of snowmelt on the marked date; light blue: the extent of the decrease in the snowmelt relative to the previous date; and orange: the extent of the increase in the snowmelt relative to the previous date.

**Table 3.** Acquisition dates of the SAR ascending and descending images used for the wet snow area detection and the results of the detected wet snow area. The reference image is the average of multiple SAR images of snow-free or dry snow-covered scenes in the fall and winter, which are not listed here.

Date	Wet Snow Area (km <sup>2</sup> )	Date	Wet Snow Area (km <sup>2</sup> )
14 May 2015–21 May 2015	8.9572	9 July 2017–14 July 2017	7.1532
7 June 2015–14 June 2015	5.2452	21 July 2017–26 July 2017	6.7004
25 July 2015–1 August 2015	3.672	31 August 2017–7 September 2017	4.8912
18 August 2015–25 August 2015	4.4884	12 September 2017–19 September 2017	5.0164
11 September 2015–18 September 2015	4.7032	16 April 2018–23 April 2018	5.728
14 April 2016–21 April 2016	9.6672	10 May 2018–17 May 2018	7.4168
8 May 2016–15 May 2016	13.5672	3 June 2018–10 June 2018	9.852
1 June 2016–8 June 2016	10.988	9 July 2018–16 July 2018	5.0184
19 July 2016–26 July 2016	6.3444	21 July 2018–28 July 2018	5.4304
12 August 2016–19 August 2016	5.9448	2 August 2018–9 August 2018	5.1408
5 September 2016–12 September 2016	6.5332	26 August 2018–2 September 2018	5.1996
9 April 2017–16 April 2017	7.09	19 September 2018–26 September 2018	6.3752
22 May 2017–27 May 2017	12.4956		

We observed the regular dynamics of the snowmelt between 2015 and 2018. Due to gaps in the SAR data collection, the state of the wet snow at the beginning of the 2015 snowmelt season could not be obtained. Although the wet snow in the entire area of Gyala Peri Peak could not be effectively detected due to the effect of shadows and layover, the overall variations in the wet snow within the basin could still be clearly illustrated. After the accumulation of snow in the basin during the winter, the state of the snow cover began to change in April, with the area of wet snow gradually increasing and the snow at lower elevations gradually melting. In the middle of May, the wet snow pixels covered most of the area of snow accumulated during the winter in the basin. The wet snow area reached its maximum extent around the middle of May, and after that, the area gradually decreased and remained stable for about two months, from late July to the end of September. In the later part of the ablation season, there were almost no wet snow pixels below 5000 m, and the wet snow was mainly distributed in the glaciated area of the Sedongpu Basin. Only a small number of wet snow pixels were located above 6000 m.

As shown in Figure 7, the variation patterns of the snowmelt within the Sedongpu Basin in 2016 and 2017 were almost the same as in 2015, with the maximum area of wet snow within the basin occurring in mid-May. Nonetheless, compared to 2015, the maximum wet snow areas in 2016 and 2017 were both significantly large. The maximum wet snow areas in 2016 and 2017 were 13.57 km<sup>2</sup> and 12.5 km<sup>2</sup>, respectively, while that in 2015 was only 8.96 km<sup>2</sup>.

Compared to the previous three years, the variation in the wet snow within the Sedongpu Basin changed significantly in 2018. The differences mainly included a slower increase in the wet snow early in the melt season and a delay in achieving the maximum wet snow area. However, more intense ablation occurred in the middle and later parts of the melt season, which caused the minimum wet snow area to be reached earlier than in the previous three years. There was an unusual increase in wet snow pixels in the later part of the melt season, with a significant increase in the wet snow pixels on Gyala Peri Peak, and more obvious melting signals were detected.

In addition, in order to analyze the variability of the wet snow changes in the snowmelt season of each year, we considered the detected wet snow pixels with their corresponding elevation values on the DEM (Figure 8). Due to the lack of a SAR dataset, the wet snow distribution in the basin during April 2015 and June and August 2017 could not be determined using SAR images, but the difference in the wet snow distribution in 2018 compared to the past three years is still distinctly illustrated in Figure 8. As the snow gradually melted, the histogram gradually centered at higher elevations. The median values in May 2018 were lower than in the previous three years, and the wet snow was mainly centered at lower elevations. In July the wet snow line rose and was higher than during the previous three years, indicating a more intense snow melting process during this period. After this, the

melting rate slowed down and returned to the same level as in the other years in August. Figure 8 also shows that there were significantly more wet snow pixels above 6500 m in 2018, and the frequency of wet snow pixels was always at a relatively high level.

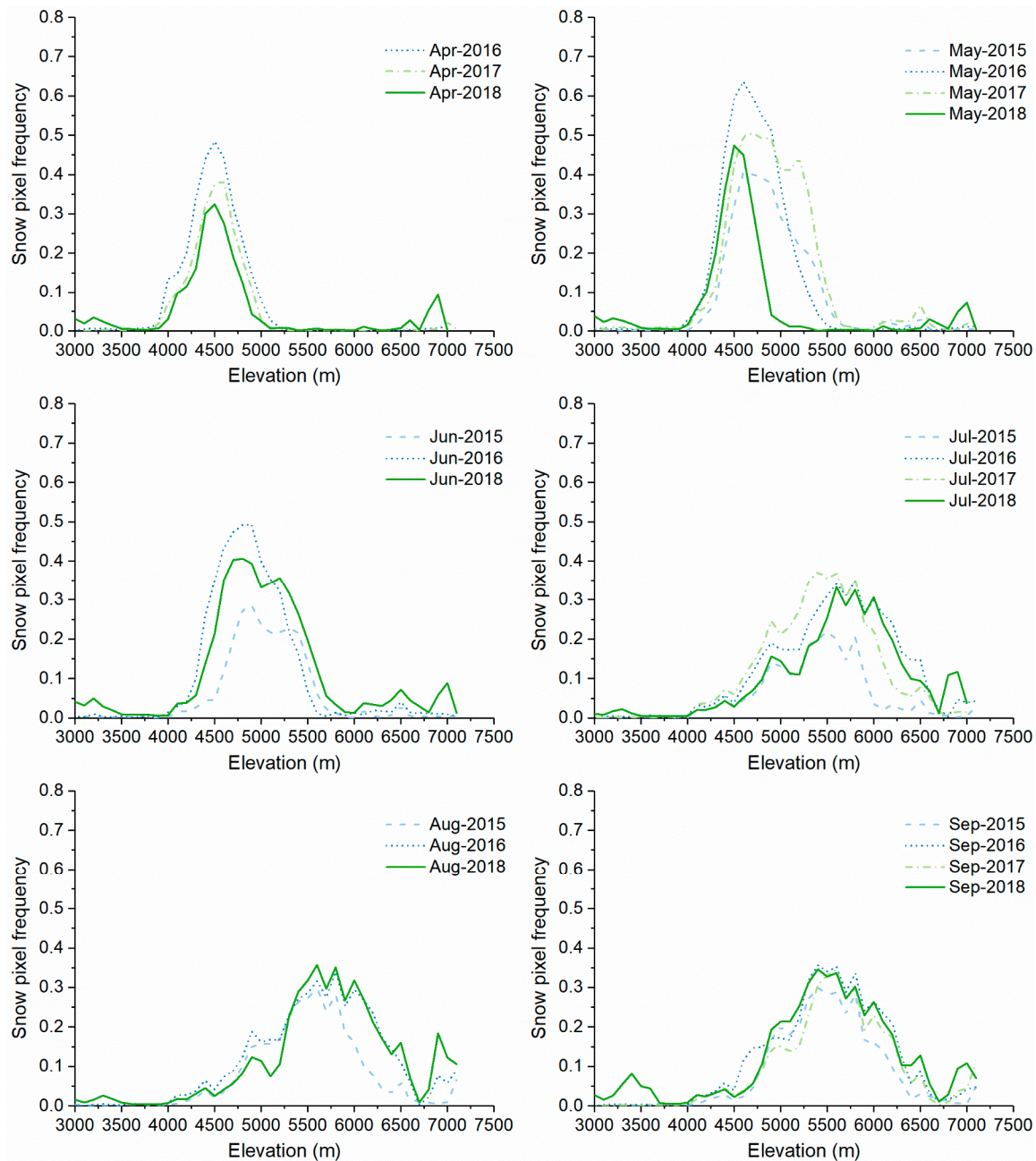


**Figure 8.** The wet snow frequency at different elevations during the snowmelt season from 2015 to 2018 based on Sentinel-1 ascending/descending images.

## 5. Discussion

### 5.1. Deformation Measured Using InSAR and Snowmelt Changes

During the period when the temperature was higher than  $0^{\circ}$  after the snowfall period, in alpine mountains, snow melt water entering the ice gap may trigger the translation of the active layer of the glacier with the bedrock, increasing the possibility of ice avalanches [34]. With increased rainfall in summer, the slope stability was greatly reduced by the mixture of the liquid water provided by the rain and snowmelt with the loose deposits. In order to further understand the triggering factors of the Sedongpu ice avalanche-induced debris

flows, the correlations between the surface deformation in the source area and the precipitation and snowmelt variations in the basin before the disaster occurred were analyzed. In order to mitigate the effect of the SAR technique in underestimating the extent of wet snow near the snow line, we calculated the average wet snow elevation to show the overall changes in the snowmelt in the basin [54]. We selected region P2 in the branch gully where ice avalanche-induced debris flows occurred and synchronized the time series of the surface deformation measured using InSAR with the daily precipitation recorded at Lulang Meteorological Station and the average elevation of the wet snow calculated in this study. It can be seen that the rainfall in the basin was mainly concentrated from June to September, with less rainfall from October to May. The total annual precipitation decreased year by year from 2015 to 2018, but it should be noted that the proportion of rainfall in the rainy season to the total annual precipitation increased, reaching 56.39% in 2018. As shown in Figure 9, we found that the increase in the cumulative deformation in region P2 was affected by both the rainfall and snowmelt, and the cumulative deformation in region P2 was significantly positively correlated with the position of the average wet snow elevation during the rainy season. After the precipitation increased in early June, the deformation in region P2 accelerated, and the snow line rose, accompanied by the gradual melting of the top layer of snow. This pattern of deformation was particularly pronounced in 2018. From early June to July 2018, persistent rainfall occurred in this area (the maximum daily rainfall during this period did not exceed 15 mm), and the rate of snow melting accelerated, with the average wet snow elevation increasing. However, the deformation rate in region P2 remained constant. Nevertheless, after a heavy rainfall event on July 9, 2018 (36.3 mm, and the maximum daily precipitation in 2018), the slope deformation accelerated significantly. During this period, as the cumulative precipitation increased, the cumulative deformation also increased. This lasted until the end of the rainy season, during which the average elevation of the wet snow area remained above 5200 m.

The start of snow melting in the year the debris flows occurred was delayed compared with that in other years. In addition, the average elevation of the wet snow in May in the other years was above 4700 m, while the average elevation of the wet snow in 2018 remained at about 4550 m. Based on the variations in the wet snow, we found that the average elevation of the wet snow increased sharply in the summer of 2018 due to an increase in temperature, therefore, it is inferred that stronger melting of snow occurred during this period than in previous years. It should be noted that in the two wet snow images acquired in September, the increase in the wet snow area from early September to late September was abnormally high, and this increase was mainly concentrated in the range of 5000–5500 m on the eastern slope. We suggest that the intense snowmelt altered the hydrological and thermal regime of the bedrock at the bottom of the ice bed and loosen the bedrock, and the loose bedrock then froze together with the glacier when the temperature decreased in October, and the bedrock was pulled up and carried away when the glacier collapsed. There were a large number of ice crevasses in the Sedongpu Basin, and the snow water generated by the rapid snow melting and the heavy precipitation in summer could easily penetrate into the glacier bed, increasing the hydrostatic pressure and reducing the friction at the bottom of the glacier, which could easily lead to glacier collapse.

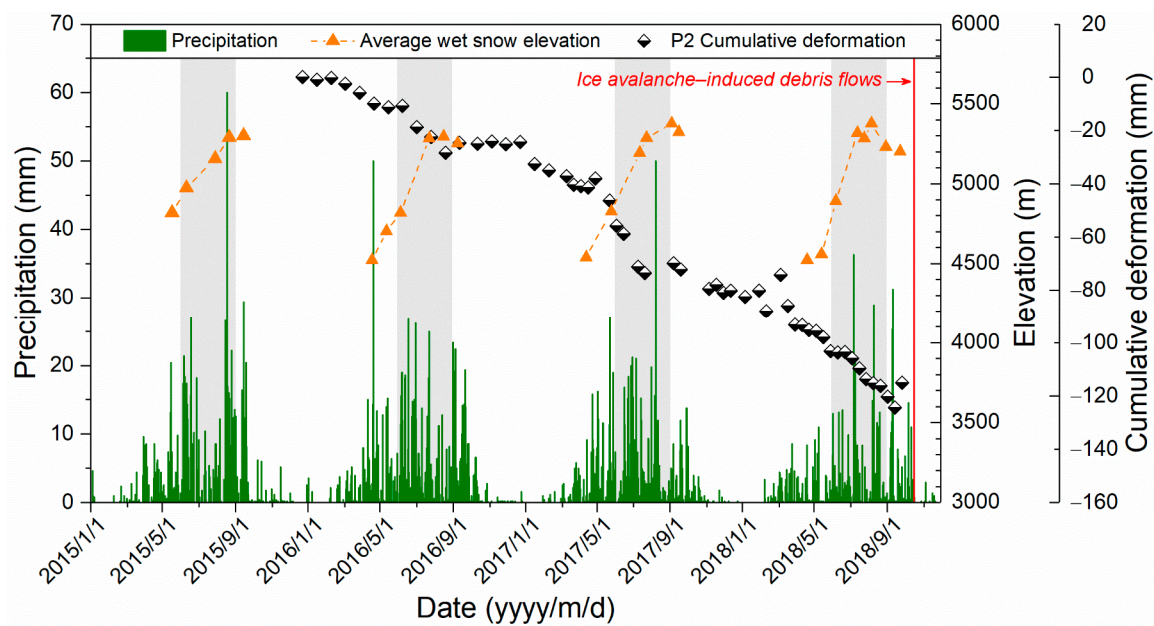


**Figure 9.** The precipitation, cumulative deformation, and average wet snow elevation before the Sedongpu ice avalanche-induced debris flows occurred. The location of P2 is shown in Figure 3. The gray shading indicates the duration of the rainy season in the basin, and the red line indicates the date of the occurrence of the ice avalanche-induced debris flows.

### 5.2. Seismic and Topographic Characteristics

The Sedongpu Basin is close to the eastern Himalayan syntaxis, which is an area of intense crustal activity and is affected by the compression and uplift of the Indian Plate and the Eurasian Plate [55]. Earthquakes occur frequently in this region due to the active tectonic movement, which reduces the stability of the surface [7]. Since 1950, a total of 294  $M_s > 3$  earthquakes have occurred in the eastern end of the Himalayas, including 26  $M_s$  3–4 earthquakes, 229  $M_s$  4–5 earthquakes, 55  $M_s$  5–6 earthquakes, and 6  $M_s > 6$  earthquakes. The most severe earthquake in this region was the  $M_s$  6.9 Nyingchi Earthquake on 18 November 2017, the epicenter of which was located 2.7 km from the NE axis of the Sedongpu Basin, with a focal depth of  $8 \pm 1.7$  km. More than a dozen aftershocks with magnitudes of about  $M_s$  4 occurred in the following month, and the successive earthquakes greatly loosened the glacial till and the material in the central part of the valley, severely reducing the stability of the glaciers with crevasses in the valley, especially those in the upper steep-slope areas of the basin.

As shown in Figure 10, the terrain of the Sedongpu Basin is a three-level stepped terrain with a steep upper terrain, flat middle terrain, and relatively steep lower terrain. A large number of glaciers have developed in the high-altitude area, and the extremely steep terrain is conducive to the development of ice crevasses on the glacier surfaces, which easily leads to the collapse of snow and ice, providing favorable conditions for the formation of large-scale mass movement events. A large amount of loose material such as glacial debris and gravel accumulates in the gently sloping middle area, which provides an abundant source of material once a movement event is initiated. The lower steep-sloped area provides the topographic conditions for the high-speed movement of debris flows, allowing the accumulation to be more conveniently transported from the source area out of the gully and to invade and subsequently cause blockage of the river channel.

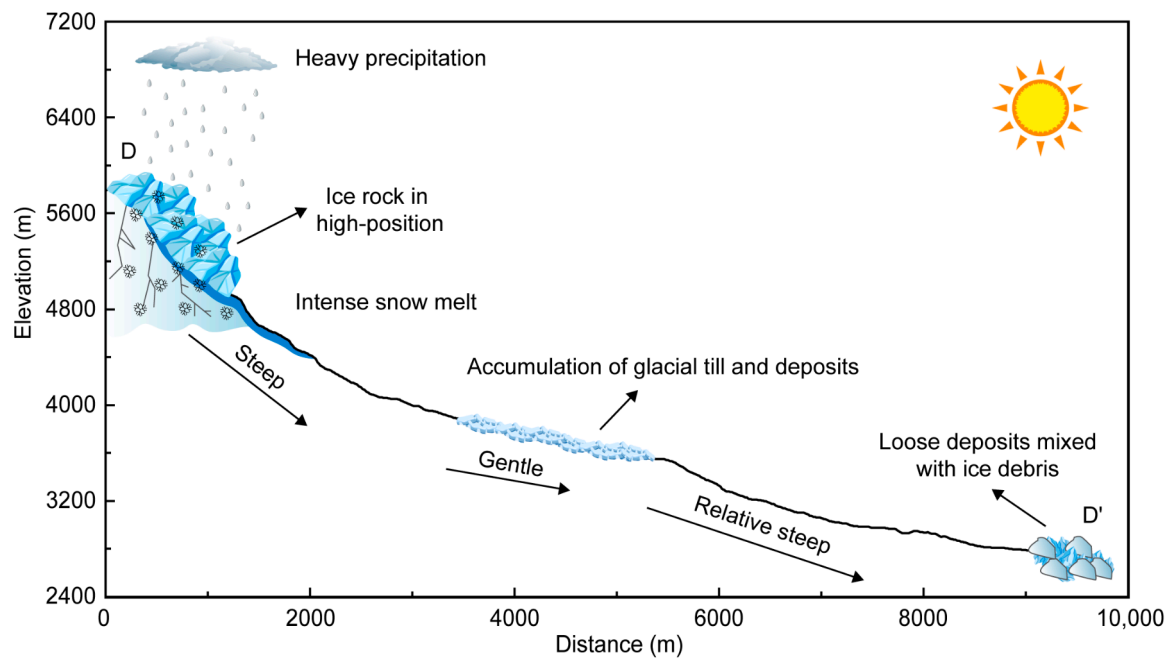


Figure 10. Schematic diagram of the Sedongpu Basin. DD' see Figure 3.

In summary, the occurrence of the Sedongpu ice avalanche-induced debris flows was the result of a combination of factors, including temperature, precipitation, earthquakes, and steep topography. The shaking caused by the earthquake destroyed the original state of the source and loose deposits, especially in the source area of the ice avalanche located at a high position. The increase in temperature led to intense melting of snow within the basin, and the snowmelt and rainfall penetrate through the ice crevices into the glacier–bedrock contact zone, generating significant water pressure at the glacier–bedrock contact, which simultaneously exerted a softening effect and promoted glacier and bedrock sliding. This eventually triggered an ice avalanche, in which the high-speed avalanche impacted and scraped the glacial till, disintegrated and mixed with the glacial till to form a high-speed debris flow. The debris flow moved downward and scraped up the glacial debris at the bottom and on both sides of the gully to form a new debris flow, which transported loose deposits mixed with ice debris into the river, leading to river blockage [7].

## 6. Conclusions

In this study, SAR images were used to retrieve the spatiotemporal changes in the pre-disaster deformation and snowmelt in the Sedongpu Basin. New insights into the causes of the ice avalanche-induced debris flows in the Sedongpu Basin were obtained through the comprehensive analysis of the time series of the variations in the deformation and snow melting before the disaster and the triggering factors. Based on the results of the InSAR analysis, the deformation in the first two years was mainly centered in the deposit accumulation area where the topography was relatively gentle. Nevertheless, the deformation characteristics of the source area changed after the Nyingchi earthquake, and the effects of the earthquake on the surface deformation were overall and large scale, especially in the steep areas. The variations in the snowmelt in the Sedongpu Basin revealed that the snow melting process in the summer of 2018 was relatively intense, which led to instability in the ice–rock zone in the Sedongpu Basin. Additionally, we found that the cumulative deformation before the ice avalanche occurred exhibited seasonal characteristics based on the relationships between the time series of the deformation and the snowmelt and precipitation data, it was found that the snowmelt and precipitation jointly affected the pre-disaster deformation. We suggest that a combination of snowmelt, rainfall, and

earthquakes, as well as climate change, ultimately triggered the Sedongpu ice avalanche-induced debris flows.

The study of InSAR deformation monitoring and wet snow monitoring based on radar remote sensing are greatly limited in temporal resolution due to the fixed revisit period of the current SAR satellites. However, precursor information such as deformation accumulation and strong snow melting obtained using SAR is crucial for monitoring mountainous areas where in situ measurements are lacking. The results of this study provide new insights into the mechanism of the ice avalanche-induced debris flows in the Sedongpu Basin, and similar events will continue to occur frequently in the future under the context of climate warming on the Tibetan Plateau. In addition, analysis based on InSAR observations and snowmelt changes can assist in disaster warning and prevention and can be applied in similar areas.

**Author Contributions:** Conceptualization, S.L. (Siyuan Luo), J.X. and W.C.; methodology, S.L. (Siyuan Luo); software, J.L.; validation, X.C. and X.W.; formal analysis, J.L.; investigation, Y.H.; resources, S.L. (Shuang Liu); data curation, Y.H.; writing—original draft preparation, S.L. (Siyuan Luo); writing—review and editing, S.L. (Siyuan Luo); visualization, H.S.; supervision, W.C.; project administration, J.X., S.L. (Shuang Liu) and K.H.; funding acquisition, J.X., S.L. (Shuang Liu) and K.H. All authors have read and agreed to the published version of the manuscript.

**Funding:** This research was funded by the National Key R&D Program of China (2020YFD1100701), the Key R&D project of the Sichuan Science and Technology Department (Grant No. 2021YFQ0042), The Science and Technology Project of Xizang Autonomous Region (Grant No. XZZ201901-GA-07), and the Strategic Priority Research Program of the Chinese Academy of Sciences (Grant No. XDA20030302).

**Data Availability Statement:** Not applicable.

**Acknowledgments:** The author would like to thank the European Space Agency for providing Sentinel-1 and -2 data. Meteorological observation data are provided by National Tibetan Plateau Data Center (<http://data.tpdc.ac.cn>, accessed on 23 December 2021).

**Conflicts of Interest:** The authors declare no conflict of interest.

## References

1. Immerzeel, W.W.; Lutz, A.; Andrade, M.; Bahl, A.; Biemans, H.; Bolch, T.; Hyde, S.; Brumby, S.; Davies, B.; Elmore, A. Importance and vulnerability of the world's water towers. *Nature* **2020**, *577*, 364–369. [[CrossRef](#)] [[PubMed](#)]
2. Yao, T.; Xue, Y.; Chen, D.; Chen, F.; Thompson, L.; Cui, P.; Koike, T.; Lau, W.K.-M.; Lettenmaier, D.; Mosbrugger, V. Recent third pole's rapid warming accompanies cryospheric melt and water cycle intensification and interactions between monsoon and environment: Multidisciplinary approach with observations, modeling, and analysis. *Bull. Am. Meteorol. Soc.* **2019**, *100*, 423–444. [[CrossRef](#)]
3. Miles, E.; McCarthy, M.; Dehecq, A.; Kneib, M.; Fugger, S.; Pellicciotti, F. Health and sustainability of glaciers in High Mountain Asia. *Nat. Commun.* **2021**, *12*, 2868. [[CrossRef](#)] [[PubMed](#)]
4. Kirschbaum, D.; Watson, C.S.; Rounce, D.R.; Shugar, D.H.; Kargel, J.S.; Haritashya, U.K.; Amaty, P.; Shean, D.; Anderson, E.R.; Jo, M. The state of remote sensing capabilities of cascading hazards over High Mountain Asia. *Front. Earth Sci.* **2019**, *7*, 197. [[CrossRef](#)]
5. Gao, J.; Yao, T.; Masson-Delmotte, V.; Steen-Larsen, H.C.; Wang, W. Collapsing glaciers threaten Asia's water supplies. *Nature* **2019**, *565*, 19–21. [[CrossRef](#)]
6. Kääb, A.; Leinss, S.; Gilbert, A.; Bühler, Y.; Gascoin, S.; Evans, S.G.; Bartelt, P.; Berthier, E.; Brun, F.; Chao, W.-A. Massive collapse of two glaciers in western Tibet in 2016 after surge-like instability. *Nat. Geosci.* **2018**, *11*, 114–120. [[CrossRef](#)]
7. An, B.; Wang, W.; Yang, W.; Wu, G.; Guo, Y.; Zhu, H.; Gao, Y.; Bai, L.; Zhang, F.; Zeng, C. Process, mechanisms, and early warning of glacier collapse-induced river blocking disasters in the Yarlung Tsangpo Grand Canyon, southeastern Tibetan Plateau. *Sci. Total Environ.* **2021**, *816*, 151652. [[CrossRef](#)]
8. Deng, M.; Chen, N.; Liu, M. Meteorological factors driving glacial till variation and the associated periglacial debris flows in Tianmo Valley, south-eastern Tibetan Plateau. *Nat. Hazards Earth Syst. Sci.* **2017**, *17*, 345–356. [[CrossRef](#)]
9. Chen, C.; Zhang, L.; Xiao, T.; He, J. Barrier lake bursting and flood routing in the Yarlung Tsangpo Grand Canyon in October 2018. *J. Hydrol.* **2020**, *583*, 124603. [[CrossRef](#)]
10. Anderson, R.S.; Anderson, L.S.; Armstrong, W.H.; Rossi, M.W.; Crump, S.E. Glaciation of alpine valleys: The glacier–debris-covered glacier–rock glacier continuum. *Geomorphology* **2018**, *311*, 127–142. [[CrossRef](#)]

11. Faillettaz, J.; Funk, M.; Vincent, C. Avalanching glacier instabilities: Review on processes and early warning perspectives. *Rev. Geophys.* **2015**, *53*, 203–224. [[CrossRef](#)]
12. Jacquemart, M.; Loso, M.; Leopold, M.; Welty, E.; Berthier, E.; Hansen, J.S.; Sykes, J.; Tiampo, K. What drives large-scale glacier detachments? Insights from Flat Creek glacier, St. Elias Mountains, Alaska. *Geology* **2020**, *48*, 703–707. [[CrossRef](#)]
13. Li, W.; Zhao, B.; Xu, Q.; Scaringi, G.; Lu, H.; Huang, R. More frequent glacier-rock avalanches in Sedongpu gully are blocking the Yarlung Zangbo River in eastern Tibet. *Landslides* **2022**, *19*, 589–601. [[CrossRef](#)]
14. Keefer, D.K. Investigating landslides caused by earthquakes—a historical review. *Surv. Geophys.* **2002**, *23*, 473–510. [[CrossRef](#)]
15. Yang, L.; Zhao, C.; Lu, Z.; Yang, C.; Zhang, Q. Three-dimensional time series movement of the cuolangma glaciers, southern tibet with sentinel-1 imagery. *Remote Sens.* **2020**, *12*, 3466. [[CrossRef](#)]
16. Yang, W.; Wang, Y.; Wang, Y.; Ma, C.; Ma, Y. Retrospective deformation of the Baige landslide using optical remote sensing images. *Landslides* **2020**, *17*, 659–668. [[CrossRef](#)]
17. Piroton, V.; Schlögel, R.; Barbier, C.; Havenith, H.-B. Monitoring the recent activity of landslides in the Mailuu-Suu Valley (Kyrgyzstan) using radar and optical remote sensing techniques. *Geosciences* **2020**, *10*, 164. [[CrossRef](#)]
18. Scaioni, M.; Longoni, L.; Melillo, V.; Papini, M. Remote sensing for landslide investigations: An overview of recent achievements and perspectives. *Remote Sens.* **2014**, *6*, 9600–9652. [[CrossRef](#)]
19. Zhou, Y.; Li, Z.; Li, J.; Zhao, R.; Ding, X. Glacier mass balance in the Qinghai–Tibet Plateau and its surroundings from the mid-1970s to 2000 based on Hexagon KH-9 and SRTM DEMs. *Remote Sens. Environ.* **2018**, *210*, 96–112. [[CrossRef](#)]
20. Ferretti, A.; Prati, C.; Rocca, F. Permanent scatterers in SAR interferometry. *IEEE Trans. Geosci. Remote Sens.* **2001**, *39*, 8–20. [[CrossRef](#)]
21. Hooper, A. A multi-temporal InSAR method incorporating both persistent scatterer and small baseline approaches. *Geophys. Res. Lett.* **2008**, *35*, L16302–L16309. [[CrossRef](#)]
22. Berardino, P.; Fornaro, G.; Lanari, R.; Sansosti, E. A New Algorithm for Surface Deformation Monitoring Based on Small Baseline Differential SAR Interferograms. *IEEE Trans. Geosci. Remote Sens.* **2002**, *40*, 2375–2383. [[CrossRef](#)]
23. Carlà, T.; Intrieri, E.; Raspini, F.; Bardi, F.; Farina, P.; Ferretti, A.; Colombo, D.; Novali, F.; Casagli, N. Perspectives on the prediction of catastrophic slope failures from satellite InSAR. *Sci. Rep.* **2019**, *9*, 14137. [[CrossRef](#)] [[PubMed](#)]
24. Dong, J.; Zhang, L.; Tang, M.; Liao, M.; Xu, Q.; Gong, J.; Ao, M. Mapping landslide surface displacements with time series SAR interferometry by combining persistent and distributed scatterers: A case study of Jiaju landslide in Danba, China. *Remote Sens. Environ.* **2018**, *205*, 180–198. [[CrossRef](#)]
25. Zhao, C.; Lu, Z.; Zhang, Q.; de La Fuente, J. Large-area landslide detection and monitoring with ALOS/PALSAR imagery data over Northern California and Southern Oregon, USA. *Remote Sens. Environ.* **2012**, *124*, 348–359. [[CrossRef](#)]
26. Dong, J.; Zhang, L.; Li, M.; Yu, Y.; Liao, M.; Gong, J.; Luo, H. Measuring precursory movements of the recent Xinmo landslide in Mao County, China with Sentinel-1 and ALOS-2 PALSAR-2 datasets. *Landslides* **2018**, *15*, 135–144. [[CrossRef](#)]
27. Intrieri, E.; Raspini, F.; Fumagalli, A.; Lu, P.; Del Conte, S.; Farina, P.; Allievi, J.; Ferretti, A.; Casagli, N. The Maoxian landslide as seen from space: Detecting precursors of failure with Sentinel-1 data. *Landslides* **2018**, *15*, 123–133. [[CrossRef](#)]
28. Kang, Y.; Lu, Z.; Zhao, C.; Zhang, Q.; Kim, J.-W.; Niu, Y. Diagnosis of Xinmo (China) landslide based on interferometric synthetic aperture radar observation and modeling. *Remote Sens.* **2019**, *11*, 1846. [[CrossRef](#)]
29. Zhang, Y.; Meng, X.; Jordan, C.; Novellino, A.; Dijkstra, T.; Chen, G. Investigating slow-moving landslides in the Zhouqu region of China using InSAR time series. *Landslides* **2018**, *15*, 1299–1315. [[CrossRef](#)]
30. Zhang, Y.; Meng, X.; Chen, G.; Qiao, L.; Zeng, R.; Chang, J. Detection of geohazards in the Bailong River Basin using synthetic aperture radar interferometry. *Landslides* **2016**, *13*, 1273–1284. [[CrossRef](#)]
31. Dunning, S.A.; Rosser, N.J.; McColl, S.T.; Reznichenko, N.V. Rapid sequestration of rock avalanche deposits within glaciers. *Nat. Commun.* **2015**, *6*, 7964. [[CrossRef](#)] [[PubMed](#)]
32. Karbou, F.; Veyssi re, G.; Coleou, C.; Dufour, A.; Gouttevin, I.; Durand, P.; Gascoin, S.; Grizonnet, M. Monitoring Wet Snow Over an Alpine Region Using Sentinel-1 Observations. *Remote Sens.* **2021**, *13*, 381. [[CrossRef](#)]
33. Ballesteros-C novas, J.A.; Trappmann, D.; Madrigal-Gonz lez, J.; Eckert, N.; Stoffel, M. Climate warming enhances snow avalanche risk in the Western Himalayas. *Proc. Natl. Acad. Sci. USA* **2018**, *115*, 3410–3415. [[CrossRef](#)] [[PubMed](#)]
34. Vergara Dal Pont, I.; Moreiras, S.M.; Santibanez Ossa, F.; Araneo, D.; Ferrando, F. Debris flows triggered from melt of seasonal snow and ice within the active layer in the semi-arid Andes. *Permafrost. Periglac. Process.* **2020**, *31*, 57–68. [[CrossRef](#)]
35. McGrath, D.; Webb, R.; Shean, D.; Bonnell, R.; Marshall, H.P.; Painter, T.H.; Molotch, N.P.; Elder, K.; Hiemstra, C.; Brucker, L. Spatially extensive ground-penetrating radar snow depth observations during NASA’s 2017 SnowEx campaign: Comparison with In situ, airborne, and satellite observations. *Water Resour. Res.* **2019**, *55*, 10026–10036. [[CrossRef](#)]
36. Edemsky, D.; Popov, A.; Prokopovich, I.; Garbatsevich, V. Airborne Ground Penetrating Radar, Field Test. *Remote Sens.* **2021**, *13*, 667. [[CrossRef](#)]
37. Nagler, T.; Rott, H. Retrieval of wet snow by means of multitemporal SAR data. *IEEE Trans. Geosci. Remote Sens.* **2000**, *38*, 754–765. [[CrossRef](#)]
38. Huang, L.; Li, Z.; Tian, B.-S.; Chen, Q.; Liu, J.-L.; Zhang, R. Classification and snow line detection for glacial areas using the polarimetric SAR image. *Remote Sens. Environ.* **2011**, *115*, 1721–1732. [[CrossRef](#)]
39. Nagler, T.; Rott, H.; Ripper, E.; Bippus, G.; Hetzenecker, M. Advancements for Snowmelt Monitoring by Means of Sentinel-1 SAR. *Remote Sens.* **2016**, *8*, 348. [[CrossRef](#)]

40. Baghdadi, N.; Gauthier, Y.; Bernier, M. Capability of multitemporal ERS-1 SAR data for wet-snow mapping. *Remote Sens. Environ.* **1997**, *60*, 174–186. [[CrossRef](#)]
41. Li, Z.; Li, B.; Gao, Y.; Wang, M.; Zhao, C.; Liu, X. Remote sensing interpretation of development characteristics of high-position geological hazards in Sedongpu gully, downstream of Yarlung Zangbo River. *Chin. J. Geol. Hazard Control* **2021**, *32*, 33–41. [[CrossRef](#)]
42. Ding, Y.; Zhang, S.; Zhao, L.; Li, Z.; Kang, S. Global warming weakening the inherent stability of glaciers and permafrost. *Sci. Bull.* **2019**, *64*, 245–253. [[CrossRef](#)]
43. Casu, F.; Manzo, M.; Lanari, R. A quantitative assessment of the SBAS algorithm performance for surface deformation retrieval from DInSAR data. *Remote Sens. Environ.* **2006**, *102*, 195–210. [[CrossRef](#)]
44. Goldstein, R.M.; Werner, C.L. Radar interferogram filtering for geophysical applications. *Geophys. Res. Lett.* **1998**, *25*, 4035–4038. [[CrossRef](#)]
45. Pepe, A.; Lanari, R. On the Extension of the Minimum Cost Flow Algorithm for Phase Unwrapping of Multitemporal Differential SAR Interferograms. *IEEE Trans. Geoenviron. Remote Sens.* **2006**, *44*, 2374–2383. [[CrossRef](#)]
46. Pepe, A.; Berardino, P.; Bonano, M.; Euillades, L.D.; Lanari, R.; Sansosti, E. SBAS-based satellite orbit correction for the generation of DInSAR time-series: Application to RADARSAT-1 data. *IEEE Trans. Geosci. Remote Sens.* **2011**, *49*, 5150–5165. [[CrossRef](#)]
47. Wu, Q.; Jia, C.; Chen, S.; Li, H. SBAS-InSAR based deformation detection of urban land, created from mega-scale mountain excavating and valley filling in the Loess Plateau: The case study of Yan'an City. *Remote Sens.* **2019**, *11*, 1673. [[CrossRef](#)]
48. Baghdadi, N.; Gauthier, Y.; Bernier, M.; Fortin, J.P. Potential and limitations of RADARSAT SAR data for wet snow monitoring. *Geosci. Remote Sens. IEEE Trans.* **2000**, *38*, 316–320. [[CrossRef](#)]
49. Nagler, T.; Rott, H.; Malcher, P.; Müller, F. Assimilation of meteorological and remote sensing data for snowmelt runoff forecasting. *Remote Sens. Environ.* **2008**, *112*, 1408–1420. [[CrossRef](#)]
50. Snehmanja; Venkataraman, G.; Nigam, A.K.; Singh, G. Development of an inversion algorithm for dry snow density estimation and its application with ENVISAT-ASAR dual co-polarization data. *Geocarto Int.* **2010**, *25*, 597–616. [[CrossRef](#)]
51. Fuhrmann, T.; Garthwaite, M.C. Resolving three-dimensional surface motion with InSAR: Constraints from multi-geometry data fusion. *Remote Sens.* **2019**, *11*, 241. [[CrossRef](#)]
52. Guo, R.; Li, S.; Chen, Y.n.; Li, X.; Yuan, L. Identification and monitoring landslides in Longitudinal Range-Gorge Region with InSAR fusion integrated visibility analysis. *Landslides* **2021**, *18*, 551–568. [[CrossRef](#)]
53. Zhao, B.; Li, W.; Wang, Y.; Lu, J.; Li, X. Landslides triggered by the Ms 6.9 Nyingchi earthquake, China (18 November 2017): Analysis of the spatial distribution and occurrence factors. *Landslides* **2019**, *16*, 765–776. [[CrossRef](#)]
54. Snapir, B.; Momblanch, A.; Jain, S.; Waine, T.W.; Holman, I.P. A method for monthly mapping of wet and dry snow using Sentinel-1 and MODIS: Application to a Himalayan river basin. *Int. J. Appl. Earth Obs. Geoinf.* **2019**, *74*, 222–230. [[CrossRef](#)]
55. Liu, C.; Chen, C. Achievements and countermeasures in risk reduction of geological disasters in China. *J. Eng. Geol.* **2020**, *28*, 375–383. [[CrossRef](#)]